

Evolution of the Galactic Globular Cluster System

Chigurupati Murali [★] and Martin D. Weinberg [†]

Department of Physics and Astronomy, University of Massachusetts, Amherst, MA 01003-4525, USA

1 February 2008

ABSTRACT

We study the dynamical evolution of disk and halo globular clusters in the Milky Way using a series of Fokker-Planck calculations combined with parametric statistical models. Our sample of 113 clusters with velocity data is predicted to descend from an initial population of 250 clusters, implying more than a factor of two decrease in population size due to evolution.

Approximately 200 of these clusters are in a halo component and 50 in a disk component. The estimated initial halo population follows a coreless $R^{-3.38}$ density profile in good agreement with current estimates for the distribution of halo field stars. The observed core in the present-day distribution of halo clusters results from the rapid evaporation of clusters in the inner regions of the Galaxy. The initial halo population is also predicted to have a radially biased orbit distribution in rough agreement with the observed kinematics of halo field stars. The isotropy of the present-day halo cluster distribution results from the evaporation of clusters on elongated orbits. Similarly, the initial disk component has a nearly isotropic initial distribution that becomes more tangentially biased with time. However, the inferred initial characteristics of the disk component do not match the kinematics of the rapidly rotating thin or thick disk stellar populations. These characteristics may be more indicative of the flattened halo component discussed by Zinn (1993).

Detailed examination of cluster evolution confirms the importance of disk heating. Clusters on low-inclination orbits experience the strongest disk heating because of optimal matches in resonant frequencies. Disk heating on high-inclination orbits is weaker but still dominates over spheroidal heating. Evaporation times depend weakly on initial concentration, density and height of oscillation above the disk.

Key words: globular clusters: general – galaxies: individual (Milky Way) – galaxies: star clusters

1 INTRODUCTION

Age estimates for globular clusters indicate that they formed early in the history of the Milky Way and represent ‘fossil relics’ of the proto-Galaxy (Larson 1990). Attempting to uncover this history, researchers have carefully examined a range of properties of the present-day cluster system, paying particular attention to the cluster kinematic distribution (e.g. Zinn 1993), mass distribution (e.g. Harris & Pudritz 1994), metallicity distribution (e.g. Zinn 1985) and age distribution (e.g. Chaboyer, Demarque & Sarajedini 1996). These investigations have provided evidence for both accreted and native components in the cluster system

(Searle & Zinn 1978) and correlations between kinematics and metallicity which may trace the collapse of the Galaxy (Zinn 1985; Armandroff 1989; Zinn 1993).

Comparisons with other stellar populations have revealed subtleties in the process of Galaxy formation and evolution. For example, in the inner Galaxy, the globular cluster distribution is flatter than the distribution of halo field stars although their profiles match well at larger radii. In addition, the field star velocity ellipsoid has a strong radial bias in comparison to the approximately isotropic cluster velocity ellipsoid (e.g. Ostriker, Binney & Saha 1989). Conversely, Zinn (1985) and Armandroff (1989) have presented convincing evidence for a high-metallicity disk cluster population which has broad similarities in kinematics, spatial distribution and metallicity with the stellar thick disk. Understanding the origin of these relationships will improve our picture of the primordial Milky Way.

[★] Present address: Canadian Institute for Theoretical Astrophysics, McLennan Labs, Toronto, ON M5S 1A1, Canada

[†] Alfred P. Sloan Foundation Fellow.

At the same time, theoretical interest in globular cluster evolution has been motivated by the discovery that two-body relaxation would drive evolution on a time scale that is much less than the age of a typical cluster (Ambartsumian 1938; Spitzer 1940; Chandrasekhar 1942). Subsequent research provided an understanding of the gravothermal instability (Lynden-Bell & Wood 1968) and the phenomenon of core collapse (e.g. Cohn 1980). One of the basic conclusions of this work on cluster evolution is that relaxation inevitably leads to evaporation (e.g. Spitzer 1987). Additional refinements to the picture of relaxation-driven evolution have been required to account for a source of energy which halts core collapse (e.g. Henon 1961; Lee & Ostriker 1987) and to include tidal influences which arise on a cluster's orbit in a parent galaxy (Ostriker, Spitzer & Chevalier 1972; Chernoff, Kochanek & Shapiro 1986; Weinberg 1994; Gnedin & Ostriker 1996; Murali & Weinberg 1996, hereafter Paper I).

Recent work on tidal influences has shown that evaporation is accelerated by the interaction of a cluster with the tidal field produced by the halo and disk of the Galaxy (Gnedin & Ostriker 1996; Paper I). These studies show that depletion depends strongly on cluster mass and orbit in the Galaxy. This suggests that understanding the initial characteristics of clusters and their relationship to other stellar populations in the Galaxy requires a comprehensive description of evolution since the time of formation. In a related study which supports this view, Murali & Weinberg (1996; hereafter Paper II), have demonstrated the importance of evolution in shaping the M87 globular cluster population and as a partial cause for the specific frequency conundrum in fundamental plane ellipticals.

Motivated by these results in the present work, we investigate the degree to which evolution has shaped the Milky Way cluster population. Our approach is to predict the initial spatial and kinematic distributions of the globular cluster system using the Fokker-Planck description of cluster evolution discussed in Paper I in combination with the parametric statistical framework employed in Paper II. The predictions describe the initial population of clusters which evolve quasi-statically through relaxation and tidal heating and indicate changes which dynamical evolution has wrought on the system as a whole. The results also provide a basis for understanding the primordial relationship of globular clusters to other stellar populations.

We first study the evolutionary behavior of clusters which inhabit the disk and halo of the Galaxy. The calculations demonstrate the importance of disk heating on cluster evolution and quantify dependences on important internal and external parameters, including orbit in the Galaxy and cluster concentration. We also examine the behavior of internal density profiles and mass spectra in evolving clusters.

Having considered the detailed physical behavior, we examine properties of the full cluster population. We first characterize properties of the current cluster population and then predict its initial conditions using the data set compiled by Gnedin & Ostriker (1996) and the three-space velocities derived by Cudworth (1993). The inferences are derived from both spherical and two-component disk+sphere models of the cluster distribution. While several analyses have shown the cluster system to be approximately spherically distributed (Chernoff & Djorgovski 1989; Thomas

1989), other investigations show two components: a flattened, rapidly rotating high-metallicity component associated with the Galactic disk and a spherically distributed low-metallicity component associated with the Galactic halo (Zinn 1985; Armandroff 1989). Further subdivisions may also exist (Zinn 1993; Zinn 1996). The choice of models reflects the gross characteristics of the cluster system and allows us to compare the candidate distributions. The results predict significant differences in the initial and present-day cluster populations, indicating the role of evolution in shaping the present-day cluster system. Moreover, neither model is completely successful in describing the cluster population probably due to the combined effects of evolution and obscuration.

The plan of the paper is as follows. In §2, we summarize the approach and scenario used throughout the investigation. The results are presented in §3 and include description of the physical behavior as a function of orbit, examination of the internal properties of evolving clusters and analysis and prediction of the initial conditions of the observed population. Finally, §4 discusses the implications of the results. The appendices provide derivations of the models and a discussion of the statistical procedure.

2 SCENARIO AND INVESTIGATION

2.1 Model populations

Our fiducial population consists of clusters which formed in a single episode approximately 11 Gyr ago, the lower limit on cluster ages estimated from current models of stellar evolution (Chaboyer 1995). For older ages, the evolution in the properties of the cluster system is greater than the estimates derived below. Initial clusters are assigned $W_0 = 5$ King model profiles. Investigation of concentration dependence in §3.1.5 shows that evaporation times vary little with W_0 . We assume that each cluster has a Salpeter IMF $m^{-\beta}$ with $\beta = 2.35$ and lower mass limit $m_l = 0.1 M_\odot$. For this choice, stellar evolution would dominate for the first Gyr, roughly corresponding to the main sequence lifetime of a $2 M_\odot$ A-star, which we choose as the upper mass limit, m_u . Following the phase of strong stellar evolution, relaxation, external heating and, ultimately, core collapse heating would begin to drive cluster evolution. We define our zero-population at this epoch, approximately 10 Gyr in the past.

In light of observational evidence, we adopt a two-component model of the cluster population consisting of flattened and spherical distributions. We employ the commonly used terminology of ‘disk’ and ‘halo’ cluster to refer to members of these sub-populations. A ‘disk’ cluster is most often ‘metal-rich’ with disk kinematics while a ‘halo’ cluster is most often ‘metal-poor’ with halo kinematics but which may have high or low orbital inclination relative to the disk. A ‘classic’ halo orbit, however, is one of high inclination from the disk.

2.2 Cluster evolution

Following formation and early stellar evolution, cluster evolution is driven by relaxation, the tidal field and binary heating of the core. As described in Papers I & II, the compe-

tition between relaxation and the tidal field of a galaxian spheroid is particularly important in determining a cluster's evolutionary time scale and survival history. The dominant effects of the spheroid on tidally-limited clusters were found to be heating on low-eccentricity orbits and tidal truncation on high-eccentricity orbits.

In the Milky Way, the disk also contributes significantly to cluster evolution. For high inclination orbits, a number of investigations have shown that the compressional shock imparted to a cluster during its passage through the disk will generally enhance the evaporation rate (Spitzer & Chevalier 1972; Chernoff, Kochanek & Shapiro 1986; Weinberg 1994; Gnedin & Ostriker 1996). For orbits confined to the disk, oscillations of the cluster about the midplane transfer energy through resonant stellar orbits. Below we examine the effect of the disk on cluster evolution on both low- and high-inclination orbits (§3.1). Appendix A outlines the derivation of the heating rate for disk oscillations.

2.3 Orbits

For eccentric, high-inclination orbits, the orbital phase of disk passage varies due to the precession of the argument of perihelion with respect to the plane of the Galaxy because orbits are not closed in the logarithmic potential. To remove dependence on orbital phase, we assume that disk shocking occurs twice per orbital period at the average orbital radius of the cluster. For eccentric low-inclination orbits, we follow the same procedure and also assume that the vertical motion is separable from the radial and tangential motion in all orbits. This allows us to define approximate three-integral distribution functions (DFs) in terms of algebraic constants of the motion (§2.5). With these DFs, we can follow the evolution of the phase space distribution of globular clusters using a series of Fokker-Planck calculations (§2.8)

Orbits in the spheroid are defined using the quantity $\kappa = J/J_{max}(E)$, the angular momentum relative to maximum for an orbit of energy E . The inclination angle, i , is defined with respect to the disk so that $i = 0^\circ$ defines an orbit in the plane of the disk. Oscillations through the disk are defined by their oscillation height in multiples of the disk scale height, z_0 .

2.4 Tidal limitation

Clusters on orbits highly inclined from the disk are tidally limited by the Galactic spheroid. While initial cluster densities may differ from the mean density required by perigalactic tidal limitation, subsequent evolution during the first gigayear leads rapidly to tidal truncation or disruption. Clusters on orbits confined to the disk may possess limiting radii, R_c , smaller than that implied by tidal limitation in the spheroid (e.g. note the discrepancy between the observed and predicted tidal radius of M71: Drukier, Fahlman & Richer 1993). This implies that their density is higher than that required for tidal limitation at given concentration. However, §3.1.3 shows that evaporation times vary little with density for fixed mass. Therefore, in studying population evolution, we assume that low-inclination clusters are also tidally limited. The limiting radius R_c is determined by the cluster mass, orbit and the ratio of cluster mean density

to the mean density required for tidal limitation (see §2.10 and Paper I for further details). When clusters are tidally limited, we refer to the limiting radius as the *tidal radius*, R_t .

2.5 Distribution functions

We use parametric models to define distributions of cluster orbits and masses in both disk and spheroid populations. Mass distributions, $\nu(M)$, are defined using either a power law (Harris & Pudritz 1994), a two-component power law or a Gaussian magnitude distribution (McLaughlin, Harris & Hanes 1994). The two-component power-law mass spectrum is continuous at the break at mass M_{cut} .

Distributions of cluster orbits are defined using well-known models (Table 1) which are generalized to provide kinematic and spatial distributions for populations in the Galactic potential (§2.9). Disk component DFs are defined as functions of E_d , the orbital energy associated with motion in the disk plane, J_z^2 , the square of the z-component of the angular momentum and E_z , the orbital energy associated with motion perpendicular to the disk plane. The functional form is obtained using the Mestel disk with no net rotation (Binney & Tremaine 1987) combined with an isothermal vertical distribution. This provides a family of constant anisotropy, power-law surface density profiles with power-law index $-(\eta_d - 2q_d)$ of infinite range. The quantities $\eta_d \equiv v_c^2/\sigma_d^2$ and q_d respectively define the velocity dispersion, σ_d , in terms of the (constant) circular rotation velocity, v_c , and degree of anisotropy of the distribution in the disk plane. The parameter $\eta_z \equiv \Phi_0/\sigma_z^2$ defines the vertical scale height of the distribution in terms of the vertical velocity dispersion, σ_z , and the central potential of the disk, Φ_0 . Appendix C discusses the model family in further detail.

Spheroidal component distribution functions are defined as functions of E , the total energy of the orbital motion, and J^2 , the square of the total angular momentum. We use two models. The first is obtained by adapting the Mestel DF to the spherical case which we refer to as the *Mestel sphere*. The second is the Eddington model (Aguilar, Hut & Ostriker 1988). The Mestel sphere provides a family of constant anisotropy power-law space density profiles with power-law index $-(\eta - 2q)$ of infinite range. The quantities $\eta \equiv v_c^2/\sigma^2$ and q respectively define the velocity dispersion, σ , in terms of the (constant) circular rotation velocity, v_c , and degree of anisotropy of the distribution as in the disk case. The Eddington sphere produces a family of variable anisotropy, power-law space density profiles with core radius R_a and power-law index $-\eta$ at large radii. Radial anisotropy becomes significant beyond the core radius. Appendices D and E provide derivations and further discussion of these models.

Complete orbit and mass distributions are given by joint distributions $\nu(M) \times f(\vec{I})$ where \vec{I} denotes constants which define a disk or halo orbit. We assume that disk and halo components can have different mass spectra. In the two-component model, F denotes the fraction of the population belonging to the spherical component. The results of §3.1 show that disk cluster evolution varies little with oscillation height. Since the cluster population is not large, we therefore determine the parameter η_z for the observed distribution, and keep it fixed when estimating the initial conditions in

order to minimize the number of parameters. For the disk distribution, we impose cutoffs in radius at $R_d = 15$ kpc (Wainscoat et al. 1992) and height at $Z = 7.5$ kpc, where R_d and Z are the radius in and height above the disk, respectively (see Appendix B for listing of coordinate notations).

2.6 Statistical procedure

A maximum likelihood method is used to estimate the parameters in Table 1 from the observed cluster data. Our models can include 7 parameters for each cluster (mass, 3 spatial coordinates and 3 velocity coordinates). However, not all quantities are available in most cases. To incorporate all available data, we use a likelihood technique for incomplete data sets (Little & Rubin 1987; Stuart & Ord 1991).

The likelihood is constructed in the usual manner as the joint probability of all observations given the model. However, for clusters with unavailable phase space quantities, the probability is obtained by integrating the distribution function over all dimensions of unknown information. This defines the marginal probability of observing a particular cluster given the model. Typically, only the heliocentric radial velocity is known, so we integrate over the tangential velocities relative to our vantage point to derive the marginal probability of observing a cluster at a given position with a given heliocentric radial velocity. Appendix F discusses the technique in more detail.

Two types of fit are used to characterize the data. Fits without the evolutionary calculations (c.f. §2.8) are used to derive the observed or *present-day* properties of the cluster sample. Fits based on the evolutionary calculations are used to derive the most likely initial conditions which produce today's distribution. We first consider the present-day characteristics of the cluster system to serve as a guide to interpreting the evolutionary case. The listed uncertainties are $1 - \sigma$ variances computed under the assumption of normally distributed errors.

2.7 Data

We use the data compiled in Gnedin & Ostriker (1996) which consists of 119 objects. Comparison with the Harris (1996) compilation shows no obvious systematic differences. We examine the distribution of clusters within 65 kpc having masses in the range $2.0 \times 10^4 M_\odot \leq M \leq 2.75 \times 10^6 M_\odot$ for a mass-to-light ratio of 3. This removes 6 clusters from the original sample, leaving a total of 113 clusters. Using the likelihood procedure outlined above, we also include the three-space velocities which now exist for about 20 clusters (Cudworth 1993). This is referred to as the *augmented data set*.

2.8 Calculations

We follow the evolution of individual clusters using the one-dimensional Fokker-Planck approximation (Cohn 1979). The calculations include relaxation, external heating due to the time-varying tidal field of the disk and spheroid, and a phenomenological binary heating term (Lee et al. 1991). Spheroidal tidal heating is included using the implementation discussed in Paper I. Disk tidal heating is implemented

as a shock on high-inclination orbits and as an average heating rate on low-inclination, oscillatory orbits. The numerical procedure used on low-inclination orbits is the same used for orbits in the spheroid. On high-inclination orbits, we use an analogous, flux-conserving scheme to compute the total change in the DF due to the passage through the disk.

Properties of the evolved cluster population are estimated from a grid of Fokker-Planck calculations performed over a range of cluster orbits. For the disk clusters, we use a $4 \times 4 \times 5$ grid in apogalactic radius, mass and κ to sample the phase space. Apogalactica are taken in the range $2 \leq R_a \leq 8$ kpc, masses in the range $10^5 M_\odot \leq M \leq 5 \times 10^6 M_\odot$ and orbits in the range $0.3 \leq \kappa \leq 1.0$. For the halo clusters, we use a $5 \times 4 \times 5$ grid with $5 \leq R_a \leq 15$ kpc and the same range of mass and κ . All clusters with $R_a = 0.8$ kpc are assumed depleted and all clusters with energies equal to a circular orbit with $R_a = 20$ kpc are assumed to be unevolved. For $R_a = 0.8$ kpc, clusters on circular orbits either evaporate or decay into the nucleus by dynamical friction (Aguilar, Hut & Ostriker 1988) and clusters on eccentric orbits evaporate. For $R_a = 20$ kpc, the evaporation timescale on a circular orbit is 70 Gyr for $10^5 M_\odot$ and is roughly the same for other orbits of equal energy. In most cases observed clusters with $M \leq 10^5 M_\odot$ initially had masses above $10^5 M_\odot$. In a few cases, extrapolation beyond the initially defined grid is required.

In §3.1, we find that low inclination halo clusters evolve more rapidly than high inclination clusters, although the differences are not extreme. However, in order to reduce computational expense, we neglect low-inclination orbits in the spherical component and assume that all orbits have high inclination. This assumption circumvents the roughly factor-of-four increase in halo phase space grid size required to sample the cylindrical geometry. As a result, the initially spherical distribution remains spherical and we underestimate the amount of evolution about the midplane of the disk. The consequences of this assumption are elaborated below.

2.9 Galactic model

We represent the spherical component of the Galaxy as a singular isothermal sphere with $V_0 = 220 \text{ km s}^{-1}$ and the disk component as an exponential disk with radial scale length $R_0 = 3.5$ kpc normalized to the disk central density in the solar neighborhood, $\rho_0 = 0.15 M_\odot / \text{pc}^3$ (Bahcall 1984). The vertical profile is taken to be Gaussian with a scale height of $z_0 = 320$ pc. The Gaussian was adopted instead of an exponential initially due to concern about the analyticity of the perturbation and its effect on adiabatic invariance. However, comparisons between the two profiles show no strong differences in heating rate (Weinberg 1994). The solar radius is taken to be $R_0 = 8.5$ kpc. All measured radial velocities are converted to velocities in the Galactic rest frame using an LSR velocity of 220 km s^{-1} and a solar motion of $(\Pi, \Theta, Z) = (-9, 12, 7) \text{ km s}^{-1}$ (Mihalas & Binney 1981).

2.10 Parameterization of disk strength

In order to parameterize the strength of the spheroid relative to the cluster in Paper I, we introduced the quantity $M(x_p)$

Table 1. Functional forms of models

Mass Models		
Name	$\nu(M) \propto$	Parameters
power law	$M^{-\alpha}$	α
two-component	$M^{-\alpha_1} (M \leq M_{cut})$	$\alpha_1,$
power law	$M^{-\alpha_2} (M > M_{cut})$	α_2, M_{cut}
Gaussian	$e^{-(V-V_0)^2/2\sigma_V^2} \cdot dV/dM$	V_0, σ_V

Distribution Functions		
Name	$f(E, J^2, E_z) \propto$	Parameters
Mestel disk	$e^{-E_d/\sigma_d^2} J_z^{2q_d} e^{-E_z/\sigma_z^2}$	$0 \leq \eta_d < \infty$ $-\frac{1}{2} \leq q_d < \infty$ $0 \leq \eta_z < \infty$
Mestel sphere	$e^{-E/\sigma^2} J^{2q}$	$0 \leq \eta < \infty$ $-1 \leq q < \infty$
Eddington sphere	$e^{-E/\sigma^2} e^{-J^2/2r_a^2\sigma^2}$	$0 \leq \eta < \infty$ $0 \leq r_a < \infty$

which denotes the fraction of the cluster mass contained within the pericentric inner Lagrange point. Here, because of the the disk, it is convenient to define the following two ratios: $\chi = x_p/R_c$ denotes the ratio of the pericentric inner Lagrange point to the limiting radius of the cluster; and $\rho_{0,d}(R)/\bar{\rho}_c$ denotes the ratio of the disk central density at a given radius R to the cluster mean density. This latter parameter defines the tidal amplitude of the disk relative to the cluster in the same way that $M(x_p)$ is used to define the relative tidal amplitude of the spheroid. Using χ , we can relate the cluster mean density, $\bar{\rho}_c$, to the mean density required for tidal limitation in the spheroid, $\bar{\rho}_t$, by $\bar{\rho}_c/\bar{\rho}_t = \chi^3$.

3 RESULTS

3.1 Physical Behavior

3.1.1 The importance of disk heating

In Paper I, the evolution of a cluster of fixed mass, $M(x_p)$ and κ could be scaled to an orbit of any energy due to the scale-free nature of the tidal field. This allowed us to compare the orbital dependence of cluster evolution in several ways using the same calculations (c.f. Paper I, §3.1). Adding the disk destroys this scaling freedom because the quantity $\rho_{0,d}(R_d)/\bar{\rho}_c$ varies with the radius of disk crossing R_d . In order to compare cluster evolution on different orbits, we show the mass remaining after 10 Gyr in tidally limited clusters on orbits of equal apocenter over a range of mass and eccentricity both with and without the disk (Tables 2 and 3).

For equal apocenter and fixed mass, the densities of tidally limited clusters increase with orbital eccentricity due to the decrease in R_t with increasing perigalactic angular frequency. Clusters on eccentric orbits therefore undergo the

most rapid relaxation and have correspondingly large evaporation rates. As a result, for evolution in the spheroid alone, the remaining masses of $10^5 M_\odot$ clusters decrease monotonically with eccentricity. Tidal heating also enhances mass loss rates on low-eccentricity orbits. The effect is noticeable in the remaining masses of more slowly relaxing $10^6 M_\odot$ clusters. At high eccentricity, relaxation still predominates, but at low eccentricity, heating becomes important. As a result there is a peak in remaining mass at intermediate eccentricity.

The large tidal amplitude of the disk relative to the spheroid greatly enhances heating on low- and intermediate eccentricity orbits in the disk+sphere calculations. High-mass low-eccentricity disk clusters lose equilibrium and disrupt. The low-mass counterparts do not disrupt but are rapidly driven to evaporation by strong tidal stripping. In addition, since the strength of the disk relative to the spheroid varies with radius, the importance of disk heating varies as a function of the radius of disk crossing. The relative strength of disk heating is highest at about 8 kpc. As a result, the $10^6 M_\odot, \kappa = 0.9$ disk cluster at 8 kpc loses more mass than does its counterpart at 4 kpc (Table 2). The tidal effect of the disk diminishes with increasing eccentricity because cluster densities increase relative to the disk density at the crossing point. Disk heating is negligible at $\kappa = 0.3$.

Halo clusters exhibit the same overall tendencies as disk clusters, but heating rates are lower because resonances are concentrated at higher frequencies than resonances due to disk oscillations. For example, at 90° inclination, the $1z_0$ passage time scale is on the order of 1 Myr while the corresponding period of an oscillation with height greater than $1z_0$ is greater than 10 Myr for a disk cluster with $R_d > 2$ kpc. The location of the resonant frequency match is significant because the increase in binding energy at higher frequency

Table 2. Disk clusters: fraction of remaining mass after 10 Gyr

$10^5 M_\odot$					
$\kappa =$	1.0	0.9	0.6	0.3	
4 kpc	0.0	0.0	0.0	0.0	disk+sphere
	0.42	0.35	0.0	0.0	sphere
8 kpc	0.0	0.0	0.05	0.0	disk+sphere
	0.77	0.76	0.40	0.0	sphere
$10^6 M_\odot$					
$\kappa =$	1.0	0.9	0.6	0.3	
4 kpc	0.0	0.54	0.74	0.60	disk+sphere
	0.77	0.84	0.89	0.60	sphere
8 kpc	0.0	0.25	0.75	0.86	disk+sphere
	0.85	0.91	0.95	0.86	sphere

for $5z_0$ oscillation height and $W_0 = 5$

Table 3. Halo clusters: fraction of remaining mass after 10 Gyr

$10^5 M_\odot$					
$\kappa =$	1.0	0.9	0.6	0.3	
5 kpc	0.14	0.10	0.0	0.0	disk+sphere
	0.58	0.55	0.0	0.0	sphere
10 kpc	0.74	0.73	0.42	0.0	disk+sphere
	0.82	0.82	0.59	0.0	sphere
$10^6 M_\odot$					
$\kappa =$	1.0	0.9	0.6	0.3	
5 kpc	0.49	0.56	0.82	0.72	disk+sphere
	0.80	0.86	0.91	0.73	sphere
10 kpc	0.80	0.82	0.90	0.90	disk+sphere
	0.87	0.93	0.96	0.90	sphere

for $i = 90^\circ$ and $W_0 = 5$

reduces the response of a stellar orbit to a perturbation of fixed amplitude.

3.1.2 Inclination dependence

The importance of resonance location and frequency matching is also evident when comparing halo clusters on orbits of different inclination with respect to the disk. Table 4 compares cluster evolution on circular orbits and shows that mass loss increases as orbits become less inclined because resonances appear at lower frequency. At 5 kpc, the best match occurs for $i = 30^\circ$, while at 10 kpc, the best match occurs at $i = 15^\circ$. Radial differences arise because the disk passage time is fixed at $1z_0/v_c \sin i$ while the cluster dynamical time scale varies as $\bar{\rho}_c^{-1/2}$ as determined by the mean density of the spheroid through tidal limitation. The drop in cluster mean density at 10 kpc leads to more efficient heating at lower passage speed.

The tendency for clusters confined to the disk and at low inclination to evolve more rapidly implies that an ini-

tially spherical halo distribution will develop a vertically-dependent density profile with minimum density about the midplane of the disk. This effect is most pronounced at low eccentricity (§3.1.1) because the high densities of tidally truncated clusters on highly eccentric orbits strongly reduce the resonance amplitudes between stellar orbits and the time-varying disk tidal field.

3.1.3 Density dependence

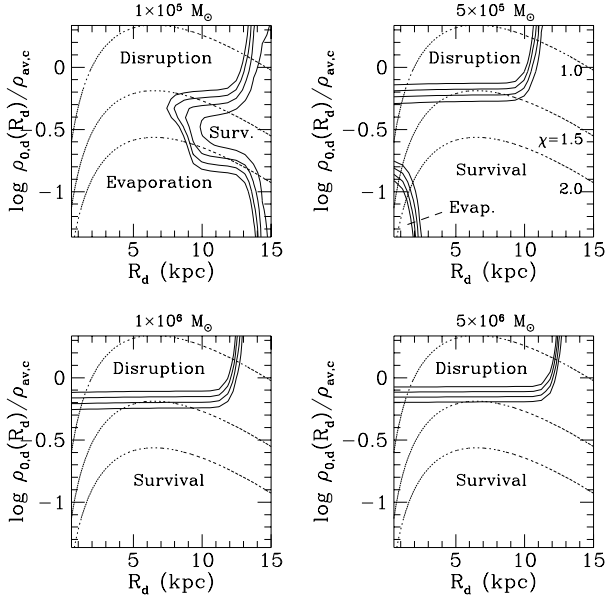
The rapid disruption of tidally-limited low-eccentricity disk clusters implies that only those with high initial densities can survive for long periods after formation. Figure 1 shows survival, disruption and evaporation patterns in clusters on circular orbits with a range of initial densities, parameterized by the ratio of disk central density to cluster mean density, $\rho_{0,d}(R_d)/\bar{\rho}_c$. The heat input from the spheroid is negligible beyond 1 kpc for disk clusters and has therefore been ignored to provide scaling freedom. Surviving clusters are bounded by disruption at low density (small χ) and evap-

Table 4. Halo clusters: fraction of remaining mass after 10 Gyr as a function of orbital inclination

$10^5 M_\odot$					
$i =$	15°	30°	60°	90°	
5 kpc	0.02	0.0	0.09	0.14	
10 kpc	0.49	0.59	0.71	0.73	

$10^6 M_\odot$					
$i =$	15°	30°	60°	90°	
5 kpc	0.50	0.41	0.44	0.49	
10 kpc	0.58	0.69	0.80	0.80	

$\kappa = 1.0$ and $W_0 = 5$

**Figure 1.** Remaining mass at 10 Gyr for disk clusters on circular orbits executing $5z_0$ oscillations as a function of the ratio of disk central density to cluster central density ($W_0 = 5$ profile). Solid contours show remaining masses in the range $3.0 \leq \log M_c \leq 4.5$ with $\Delta \log M_c = 0.5$. Dotted contours show values of χ as labeled in the top right panel. Initial masses are given at the top of each panel. Lower density clusters tend to disrupt due to tidal heating while higher density clusters tend to evaporate due to rapid rates of relaxation. The density required for tidal limitation in the spheroid is too low to allow survival against disk heating.

oration at high density (large χ). Clusters with $10^5 M_\odot$ can only survive for $R_d > 7$ kpc. For higher mass, the evaporation boundary moves to higher density because of the longer relaxation time scale. However, the disruption boundary remains roughly constant at density higher than the tidal limit.

3.1.4 Dependence on oscillation height

Table 5 shows the dependence of disk cluster evolution on oscillation height for clusters on circular orbits with $\log \rho_{0,d}(R_d)/\bar{\rho}_c = -0.37$. This value is well within the tidal

limit set by the spheroid for $R_d > 1$ kpc but still strongly influenced by disk heating. Evolution is weakly dependent on the oscillation amplitude, with the maximum effect occurring between $2z_0$ and $5z_0$. We exploit this property below to remove the vertical dimension from the phase space grid used to construct the distribution of evolved disk clusters.

3.1.5 Concentration dependence

The preceding discussion is based on clusters of a single concentration. To examine the concentration dependence, we consider the evolution of disk clusters of varying concentration for a range of mass and at values of $\rho_{0,d}(R_d)/\bar{\rho}_c$ which bracket the range of maximum cluster lifetime. Figure 2 indicates that evaporation dominates at high concentration and high density while disruption dominates at low concentration and low density. Clusters show similar trends for increasing eccentricity, with evaporation becoming more important due to the increasing densities of tidally limited clusters at fixed Galactocentric radius.

3.2 Internal properties

To illustrate some basic trends in the evolution of internal cluster properties, we examine traits of the $10^6 M_\odot$ disk clusters with apogalactica at 8 kpc. Figure 3 compares evolution in projected profiles for cases ranging from tidal disruption to relaxation-dominated core contraction. The tidally dominated $\kappa = 1.0$ and $\kappa = 0.9$ clusters shows marked departure from the initial profiles, developing a steeper, roughly power-law decline. The limiting radii remain near the expected tidal boundary which moves inward due to the mass loss. For $\kappa = 0.7$, heating is strong enough to produce deviation from the initial King profile, although the central evolution is relatively unaffected. For $\kappa = 0.5$, heating is so weak that the outer profile remains fixed while the central regions undergo gravothermal contraction. The tidally influenced profiles also show mild concavity in the fall-off, a feature which resembles the observed profiles given by Grillmair et al. (1995,1996), who interpreted their observations as *tidal tails*. However, the feature evident here is not an unbound tidal tail but a bound halo region which has been partially cleared through orbital resonances.

The evolution of the profile of the mass spectral index is shown in Figure 4. Mass segregation occurs in every case,

Table 5. Disk clusters: fraction of remaining mass after 10 Gyr as a function of disk oscillation height

		oscillation height			
		$1z_0$	$2z_0$	$5z_0$	$10z_0$
$10^5 M_\odot$	4 kpc	0.0	0.0	0.0	0.0
	8 kpc	0.45	0.36	0.38	0.43
$10^6 M_\odot$	4 kpc	0.80	0.76	0.67	0.69
	8 kpc	0.82	0.81	0.77	0.78

$\kappa = 1.0$ and $W_0 = 5$

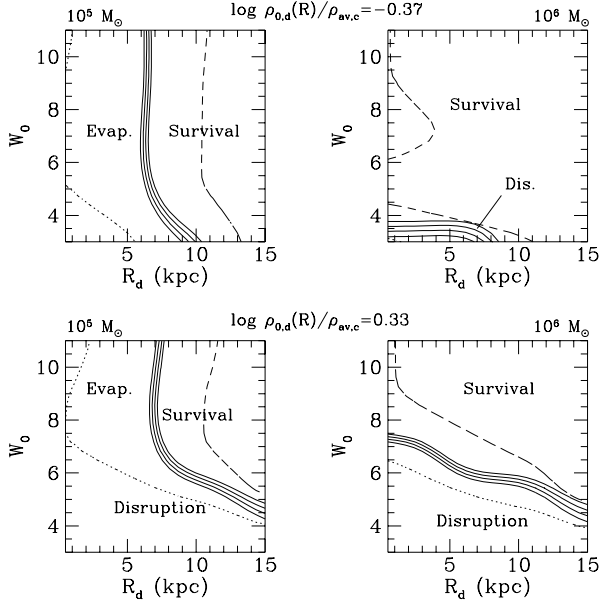


Figure 2. Remaining mass after 10 Gyr as a function of initial concentration and radius in the disk for clusters on circular orbits with indicated masses and mean densities. Solid contours show remaining masses in the range $3.0 \leq \log M_c \leq 4.5$ with $\Delta \log M_c = 0.5$. Evaporation/disruption isochrones at 5 Gyr (dotted) and 15 Gyr (dashed) are also shown. Clusters with $10^5 M_\odot$ evaporate for $R_d \leq 6$ kpc at high mean density (upper left) and evaporate or disrupt for $R_d \leq 7$ kpc at low mean density (lower left). Clusters with $10^6 M_\odot$ disrupt for $R_d \leq 7$ kpc and very low concentration at high mean density (upper right) and disrupt over a large range in radius and concentration for low mean density (lower right).

regardless of the strength of tidal heating. Most low-mass stars evaporate while the $\kappa = 1.0$ cluster disrupts as indicated by the strong flattening of $\beta(R)$ at all radii. The other cases show flattening of the spectrum in the core and steepening in the halo with differences that increase with eccentricity. The increasing differences result from the shorter evolutionary time scales at high eccentricity for orbits with equal apocenter. Aside from differences in time scale, the evolution of the mass spectral index does not depend significantly on orbit. The spectral index remains approximately constant in time near the initial half-mass radius of the cluster. However, the half-mass radius is relatively constant only in the most eccentric cases and undergoes considerable evolution where tidal effects are strong.

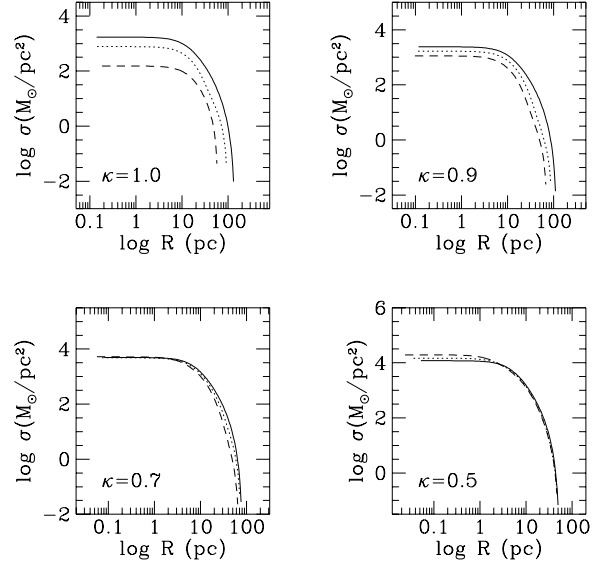


Figure 3. The evolution of surface density profiles in four $10^6 M_\odot$ clusters on indicated orbits with apogalactica at 8 kpc. Solid lines show initial profiles; dotted lines show profiles after 5 Gyr; dashed lines show profiles after 10 Gyr except for $\kappa = 1.0$ whose profile is shown at 7.5 Gyr, just prior to disruption. In the strong tidal cases ($\kappa = 1.0, \kappa = 0.9$), halos are truncated and profiles develop a steeper fall off than the initial profile. In the $\kappa = 0.7$ case, no expansion occurs due to the near balance between heating and relaxation, but the outer profile evolves due to tidal heating. The $\kappa = 0.5$ cluster undergoes negligible tidal heating, evidenced by the static halo profile, while relaxation leads to increasing central densities.

3.3 Characteristics of the present-day cluster population

3.3.1 Distribution of cluster masses

The mass spectrum of observed clusters is not well-described by a single power-law index over the mass range considered here. Harris & Pudritz (1994) find a change in slope near $10^5 M_\odot$. This trend is evident in Table 6 which compares fits to the mass spectrum using three different models: a single power law, a two-component power law and a Gaussian magnitude distribution. The single power law shows a relatively flat spectrum in agreement with Harris & Pudritz (1994). The two-component power law shows a fairly steep dependence for $M > 2.2 \times 10^5 M_\odot$ and a nearly flat spectrum for masses below that. The Gaussian magnitude distribution

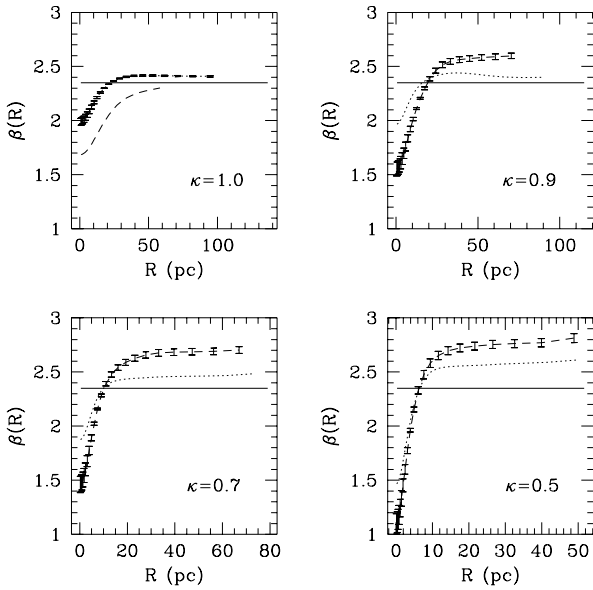


Figure 4. The line-of-sight mass spectral index as a function of projected cluster radius. Solid lines show the initial value, $\beta = 2.35$; dotted lines show the dependence after 5 Gyr; dashed lines show the dependence after 10 Gyr, except for $\kappa = 1.0$ which shows $\beta(R)$ after 7.5 Gyr, just prior to disruption. Uncertainties are plotted in only one case to show the typical size of $1 - \sigma$ error bars. The index $\beta(R)$ shows the effect of mass segregation in each case. The increased difference between core and halo indices with eccentricity results from the more rapid evolutionary timescale at high eccentricity for orbits with equal apocenter.

peaks at $2.7 \times 10^5 M_{\odot}$, consistent with the two-component power law.

Likelihood ratio tests show that the single power law can be rejected in favor of both the Gaussian magnitude distribution and two-component model at better than 99% confidence. The Gaussian and two-component power law can be discriminated with only 40% confidence. However, because the data is so sparse, we adopt the single power law as the simplest model which provides a tenable description of the overall cluster mass distribution.

3.3.2 Orbital dynamics and spatial distribution

Figure 5 shows the inferred model parameters for the Mestel sphere both with and without the tangential velocities. The comparison shows the improved constraints that the additional information provides. With the radial velocity data set, the tangential anisotropy of the Mestel sphere fit is unconstrained; in the augmented data set, the confidence contours close within $q = 1.0$ and $\eta = 5.0$ at 99% confidence. The contours are centered about isotropy and rule out strong anisotropy. We will use the augmented data set throughout the remainder of this paper.

The estimated value of the anisotropy radius of the Eddington sphere, $R_a = 20$ kpc (Table 7), also indicates an isotropic distribution. A likelihood ratio test weakly favors the Eddington sphere over the Mestel sphere with 75% confidence. The better fit results primarily because the Ed-

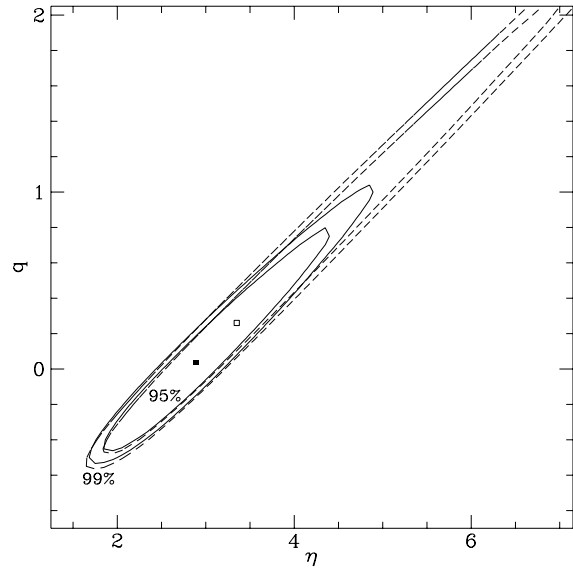


Figure 5. Comparison of Mestel sphere fits to data with (solid) and without (dashed) available three-space velocities. The additional information in the augmented data set provides some constraint on the degree of tangential anisotropy compared to the pure radial velocity data. The uncertainty still dominates, but we can rule out strongly anisotropic distributions.

dington sphere has a central core and a steep decline for $R > 20$ kpc. However, as shown in Paper II, cluster distributions probably follow steep power-law profiles initially and develop cores at later times through dynamical evolution. Both models can provide nearly coreless power-law density profiles, but the Eddington sphere becomes extremely radially biased in this case. The Mestel sphere, by contrast, can have arbitrary orbital anisotropy for a given spatial profile. Therefore, considering the relative isotropy of the present-day population, the Mestel sphere provides a more realistic description of an initial cluster population. To investigate initial conditions below, we use only the Mestel sphere to model the spherical portion of the cluster distribution.

The two-component analysis implies that 96% of the clusters are in a spherical component, according to the estimated value of F (Table 8). The inferred sphericity of the distribution is in agreement with previous analyses of the full cluster system (Frenk & White 1980; Thomas 1989; Chernoff & Djorgovski 1989). However, a likelihood ratio test rejects both the Mestel and Eddington spheres in favor of the two-component model at better than 99% confidence, indicating that the purely spherical models inadequately represent the dynamics of the full system. The preference stems from the strong tangential anisotropy attributed to the disk component.

Strong tangential anisotropy is expected in a disk component due to the presence of the rapidly rotating system of high-metallicity disk clusters (Armandroff 1989). However, our estimate implies that only 4 clusters in the sample are associated with the disk, while recent determinations indicate the presence of nearly 25 metal-rich disk clusters (Armandroff 1993). This apparent contradiction may result from the

Table 6. Models of present-day mass spectrum

Model	α_1	σ_{α_1}	α_2	σ_{α_2}	$M_{cut}(M_{\odot})$	$\sigma_{M_{cut}}$	log L
power-law	0.80	0.05	-	-	-	-	-260.56
two-component							
power-law	0.034	0.15	1.62	0.15	2.2×10^5	2.6×10^4	-248.38

Model	V_0	σ_{V_0}	σ_V	σ_{σ_V}	log L
gaussian mag.	-7.56	0.11	1.30	0.10	-251.03

Table 7. Comparison of fits to Mestel and Eddington spheres.

Model	η	σ_{η}	q	σ_q	r_a	σ_{r_a}	log L
Mestel	2.89	0.25	0.04	0.11	-	-	-3544.4
Eddington	2.54	0.10	-	-	20.1	4.1	-3542.3

obscuration of low-latitude clusters and the greater evolutionary rate of clusters near the disk (§3.1.2), both of which lead to a deficit of halo clusters near the disk. As a result, the ‘hole’ in the spherical component is filled by ‘borrowing’ the isotropic portion of the disk system which is kinematically well-matched to the halo system. This leaves a residual system of disk clusters with very high angular momentum.

3.4 Initial conditions of the cluster population

Evolution of the pure Mestel sphere produces a profile which is shallower at present than in the past (Figure 6) due to the more rapid evolution at small galactocentric radii. The initial velocity distribution is tightly constrained to isotropic.

Table 9 compares the best-fit parameters of the spherical model with the two-component model. The spheroid in the two-component model has a slightly shallower decline but is considerably more radially biased because higher angular momentum orbits are mainly associated with the disk. The uncertainties in the disk parameters are reduced because the present-day population fraction $(1-F)$ is larger than in the present-day model. The current population is estimated to number about 16 clusters. This is still somewhat below the expected size, but again may be the result of imposing spherical symmetry on the evolved halo distribution. A likelihood ratio test rejects the purely spherical model with 97.5% confidence.

The analysis predicts that the velocity distributions of both halo and disk components become more tangentially biased with time due to the more rapid evaporation of clusters on eccentric orbits. The initial orbit distribution of the halo component has fairly strong radial bias, with approximately 41% of its kinetic energy in radial motion, while the disk component has a nearly isotropic initial orbit distribution. In addition, the initial halo cluster density distribution has power law index of $\eta - 2q = 3.38$, while the disk cluster density distribution has power law index $\eta_d - 2q_d = 2.25$.

Figure 7 compares the cumulative distribution of clusters in our data sample with the evolved profile of the two-component model along with the separate contributions of the disk and sphere. The model matches the data fairly well. At small radii our models overestimate the expected number

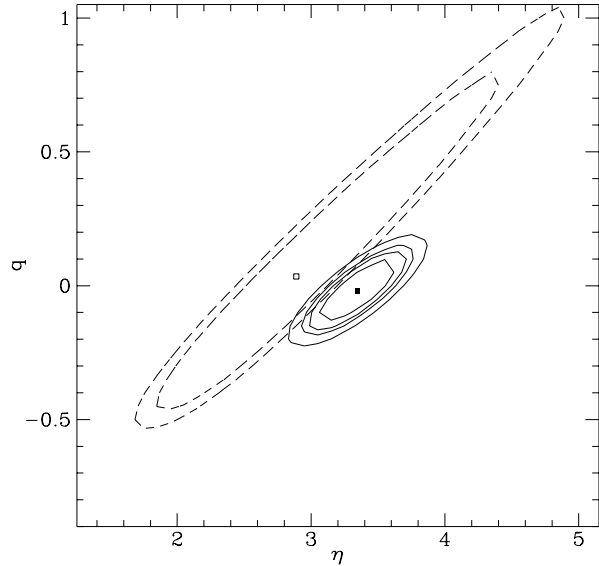


Figure 6. Comparison of 50%,90%,95%,99% confidence levels in estimated initial parameters (solid) with levels in estimated present-day parameters superimposed from previous figure (dashed). Constraints are stronger on the initial distribution and indicate initial isotropy. The slope of the initial density distribution $-(\eta + 2q)$ is approximately $r^{-3.35}$ while the present-day slope is best described as $r^{-2.95}$.

of clusters. However, the KS confidence that the observed and model distribution differ is only 58%.

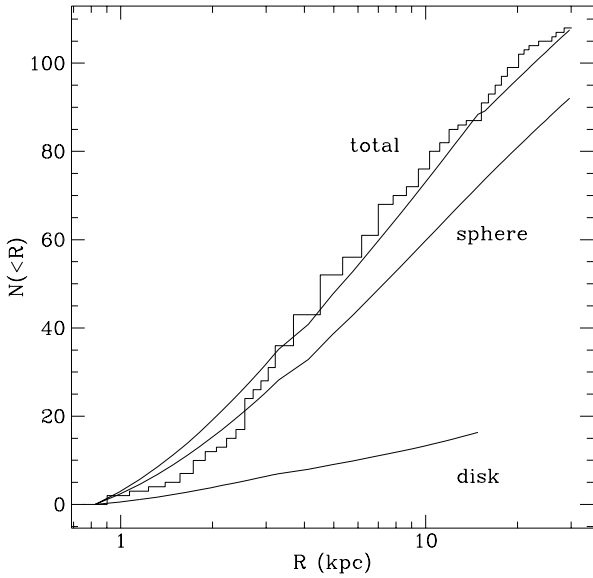
Using the initial conditions from the two-component model, we derive the estimated initial distribution of clusters (Figure 8). The total initial population has roughly 250 clusters, with 200 in the spheroid and 50 in the disk. Approximately 43% of the initial population remains.

Table 8. Present-day two-component model

	η	q	α	η_d	q_d	η_z	α_d	F	$\log L$
estimate	2.75	-0.035	0.76	17.0	7.8	0.37	1.04	0.96	-3495.00
uncertainty	0.24	0.12	0.05	7.08	3.34	0.16	0.13	$+0.04$ -0.10	-

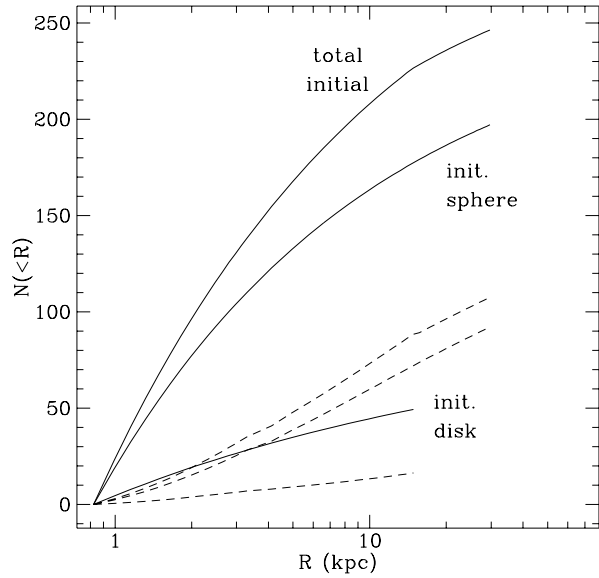
Table 9. Comparison of initial conditions in 2-component and spherical models

	spherical							
	η	q	α	η_d	q_d	α_d	F	log L
estimate	3.35	-0.018	0.95	-	-	-	-	-3486.94
uncertainty	0.32	0.16	0.06	-	-	-	-	-
	2-component							
	η	q	α	η_d	q_d	α_d	F	log L
estimate	2.82	-0.28	0.96	2.38	0.066	1.15	0.89	-3478.79
uncertainty	0.27	0.03	0.07	0.53	0.10	0.23	0.08	-

**Figure 7.** Comparison of the evolved two-component model with the observed cumulative distribution of clusters with $R < 30$ kpc in the present sample. The total number of clusters is 108. The spherical component is estimated to have 92 clusters and the disk 16.

4 DISCUSSION

Before significant mass loss through stellar evolution, young clusters typically have strongly concentrated profiles (e.g. Elson, Fall & Freeman 1987). During this phase, concentration is reduced as mass loss dominates gravothermal contraction, driving the expansion of individual clusters (Chernoff & Weinberg 1990). When stellar evolution mass loss subsides—and our model calculations begin—the resulting population will consist of clusters with a range of profiles. The calculations shown in §3.1.5 indicate, however, that evaporation times do not strongly depend on initial concentration. High concentration clusters undergo weaker tidal heating

**Figure 8.** Comparison of initial (solid) and evolved (dashed- from previous figure) two-component models. The total initial number of clusters is estimated to be about 250 with 200 in the spheroid and 50 in the disk.

but maintain correspondingly larger rates of relaxation, so that evaporation times, for given mass, are approximately independent of concentration. The weak dependence of evaporation time on density is similar (§3.1.3). The results of our calculations, therefore, do not depend significantly on the distribution of initial concentration.

Estimates of initial population size are derived assuming that an initially spherical cluster distribution remains spherical. However, clusters on orbits confined near the disk evolve more rapidly than those on high inclination orbits, leaving an axisymmetric distribution with minimum density about the midplane of the disk. Estimates of initial halo cluster population size should not change significantly when

accounting for additional cluster loss at low inclination because only $\sim 10\%$ more depletion of halo clusters is required to account for the remaining disk clusters. However, the observed disk cluster population is about 60% larger than our estimate of 16. Assuming that our estimate for the initial population size scales accordingly, we estimate that the disk population may have had roughly 80 members initially.

The choice of the mass spectrum of clusters also influences estimates of initial population size. While use of a single power law is necessitated by sample size, the two-component power law clearly provides the best fit. To gauge the importance of this choice, we use the two-component fit and the results of Paper II as a guide. We estimate that the spectral index may decrease by 0.2 for $M \gtrsim M_{cut}$ and by 0.3 for $M \lesssim M_{cut}$ since the high mass range is very similar to that considered in Paper II while more rapid evolution occurs in the low mass range. This implies initial spectral indices of $\alpha_1 = 0.3$ and $\alpha_2 = 1.8$ and 49% of the population with $M \leq M_{cut}$. In the single index fit with $\alpha = 0.95$, 47% of the population has $M \leq M_{cut}$. Since most of these clusters evaporate within a Hubble time and since they dominate the depleted population, estimates of initial size will not change substantially when using a two-index model.

Both the spatial and kinematic distributions of halo globular clusters differ from those of halo field stars. Harris (1976) and Zinn (1985) found that the spatial distribution of the full cluster system goes as $R^{-3.5}$ for $4 \leq R \leq 20$ kpc, in good agreement with the profile of halo field stars (Freeman 1996). At smaller radii the profile becomes shallower and flattens into a core (Ostriker, Binney & Saha 1989). Similarly, while the distribution of halo field star orbits appears to have significant radial bias (Beers & Sommer-Larsen 1995), the distribution of halo cluster orbits appears to be nearly isotropic (§3.3.2). Our results from the present-day fits also exhibit the discrepancy between the spatial distributions of halo clusters and halo field stars. The power-law profile derived using the Mestel sphere appears considerably flatter than $R^{-3.5}$ because we have included clusters with $R \leq 4$ kpc in the data set. The Eddington sphere best represents the distribution over the full radial range. It has a core, density $\rho \propto R^{-2.5}$ at small radius, a steep drop beyond 20 kpc with density $\rho \propto R^{-4.5}$ and the expected power-law decline with density $\rho \propto R^{-3.5}$ at intermediate radii.

Based on the estimates of initial conditions, we conclude that cluster evolution can account for the difference between the spatial distributions of halo clusters and field stars. The estimated initial density profile $\rho \propto R^{-3.38 \pm 0.3}$ in both spherical and two-component models over the full radial range of the data. This is in good agreement with the halo field star profile $\rho \propto R^{-3.29 \pm 0.24}$ recently determined by Sommer-Larsen & Zhen (1990) as well as the conventionally accepted value of $R^{-3.5}$.

Evolution also accounts for at least some differences in halo cluster and field star kinematics. As discussed in §3.4, the predicted initial halo cluster population in the 2-component model has a strong radial bias which diminishes over time due to the preferential evaporation of clusters on eccentric orbits. Approximately 41% of the kinetic energy of this component is initially in radial motions. Compared to 33% implied by the isotropy of the observed halo cluster distribution, this is closer to the value of 54% derived for halo

field stars by Beers & Sommer-Larsen (1995) and is roughly consistent with the value of 44% derived by Norris (1986).

The predicted initial disk population, by contrast, is unlike the observed stellar thick disk. The estimates indicate that the present-day high angular momentum population developed from a nearly isotropic initial distribution through the selective evaporation of clusters on eccentric orbits. Although the model underestimates the size of the disk population, any resulting kinematic bias predicts higher angular momentum in the system because lower angular momentum members cannot be distinguished from the halo clusters. Evidence for a flattened component with nearly random kinematics may exist in the sample of halo clusters studied by Zinn (1993) and in the halo field star sample studied by Sommer-Larsen & Zhen (1990).

Overall, the results of this paper point to a scenario which correlates the origin of halo field stars and clusters during Galaxy formation. The predicted disk cluster system is less clearly correlated with observed disk stellar populations but may be related to an intermediate phase of the dissipative collapse which is thought to have given rise to the disk (Larson 1990; Zinn 1993). The results do not contradict merger-induced heating of an initially cold disk (Quinn, Hernquist & Fullager 1993), provided that initially circular disk cluster orbits can be isotropized by the accretion event.

Finally, we emphasize that our predictions describe the initial population of clusters which evolve quasi-statically through relaxation and tidal heating. Since clusters probably formed with a range of initial densities, some would have been prey to rapid tidal disruption (Paper I). However, the significance of such initial conditions cannot be divined from the observed population because, excepting a few clusters such as Pal 5 (Cudworth 1993), the majority of observed clusters must have formed with initial densities which allowed quasi-static evolution and long-term survival. Consequently, the importance of tidal disruption in shaping the cluster population at an early epoch can be described only through models of the initial conditions of the cluster system in a proto-Galactic or cosmological context (Paper I).

5 CONCLUSIONS

The main conclusions of this work are as follows:

- (i) The disk dominates tidal heating on low-eccentricity orbits. The effect of the spheroid is negligible except for $R \lesssim 1$ kpc.
- (ii) Disk oscillations heat more efficiently than disk shocking due to better frequency matching in typical cluster potentials.
- (iii) Cluster evolution depends weakly on initial concentration and density due to the combined effects of tidal heating and evaporation.
- (iv) The evolution of disk clusters depends weakly on oscillation height.
- (v) The loss of clusters on low-inclination orbits implies that the distribution of halo clusters is less dense near the disk.
- (vi) The evaporation of clusters on high-eccentricity orbits leads to increasing tangential bias in the distribution of cluster orbits.

(vii) The estimated initial spatial distribution of halo clusters matches the present-day distribution of halo field stars. The estimated initial kinematic distribution is nearer to the observed radial anisotropy in the kinematics of halo field stars, having approximately 40% of its energy in radial motions.

(viii) The estimated initial distribution of disk clusters does not match the kinematic distribution of the stellar disk. However, it is similar to the flattened halo samples studied by Zinn (1993) and Sommer-Larsen & Zhen (1990).

(ix) The outer profiles of evolving clusters deviate from the initial profiles in cases of moderate to strong tidal heating, leading to considerable evolution in the half-mass radius. Profiles may also show density inflections which result from resonant clearing and which resemble the observed profiles of Grillmair et al. (1995, 1996).

(x) Profiles of the mass spectral index become flatter in the core and steeper in the halo due to mass segregation. The profiles evolve similarly on all orbits and differ at fixed times only through orbitally determined differences in evolutionary timescale.

ACKNOWLEDGEMENTS

This work was supported in part by NASA award NAGW-2224.

REFERENCES

- Aguilar, L., Hut, P. & Ostriker, J. P. 1988, *ApJ*, 335, 720
 Ambartsumian, V. A. 1938, *Ann Leningrad State U.*, no 22 [translated in Goodman & Hut 1985]
 Armandroff, T., 1989, *AJ*, 97, 375
 Armandroff, T., 1993, in *The Globular Cluster-Galaxy Connection*, eds. Smith, G. H. & Brodie, J. P. (Astr. Soc. Pacific: San Francisco), 48
 Bahcall, J. N. 1984, *ApJ*, 287, 926
 Barnes, J., Goodman, J. & Hut, P. 1986, *ApJ*, 300, 112
 Beers, T. C. & Sommer-Larsen, J. 1995, *ApJS*, 96, 175
 Binney, J. J. & Tremaine, S. D., 1987, *Galactic Dynamics* (Princeton: Princeton University Press)
 Chandrasekhar, S. 1942, *Principles of Stellar Dynamics* (Chicago: University of Chicago Press)
 Chaboyer, B. 1995, *ApJ*, 444, L9
 Chaboyer, B., Demarque, P. & Sarajedini, A., 1996, *ApJ*, 459, 558
 Chernoff, D. F., Kochanek, C. S. & Shapiro, S. L. 1986, *ApJ*, 309, 183
 Chernoff, D. F. & Djorgovski, S. D. 1989, *ApJ*, 339, 904
 Chernoff, D. F. & Weinberg, M. D. 1990, *ApJ*, 351, 121
 Cohn, H. N. 1979, *ApJ*, 234, 1036
 Cohn, H. N. 1980, *ApJ*, 242, 765
 Cudworth, K. M., 1993, in *Galaxy Evolution: The Milky Way Perspective*, ed. Majewski, S. R. (Astr. Soc. Pacific: San Francisco)
 Drukier, G. A., Fahlman, G. G. & Richer, H. B. 1992, *ApJ*, 386, 106
 Elson, R. A. W., Fall, S. M. & Freeman, K. C. 1987, *ApJ*, 323, 54
 Freeman, K. C. 1996, in *Formation of the Galactic Halo...Inside and Out*, eds. Morrison, H. & Sarajedini, A. (Astr. Soc. Pacific: San Francisco), 3
 Frenk, C. S. & White, S. D. M. 1980, *MNRAS*, 193, 295

- Gnedin, O. & Ostriker, J. P. 1996, *ApJ*, submitted
 Grillmair, C. J., Ajhar, E. A., Faber, S. M., Baum, W. A., Holtzman, J. A., Lauer, T. R., Lynds, C. R. & O'Neil, Jr., E. J. 1996, *AJ*, 111, 2293
 Grillmair, C. J., Freeman, K. C., Irwin, M. & Quinn, P. J. 1995, *AJ*, 109, 2553
 Goodman, J. & Hut, P. eds. 1985, *Dynamics of Star Clusters*, IAU Symposium 113 (Dordrecht: Reidel)
 Harris, W. E. 1976, *AJ*, 81, 1095
 Harris, W. E. 1996, *Catalog of Parameters for Milky Way Globular Clusters*, <http://www.physics.mcmaster.ca/Globular.html>
 Harris, W. E. & Pudritz, R. E. 1994, *ApJ*, 429, 177
 Henon, M. 1961, *Ann. d'Astrophys.*, 24, 369
 Henon, M. 1973, *A&A*, 24, 229
 Larson, R. B. 1990, *PASP*, 102, 709
 Lee, H. M., Fahlman, G. G., & Richer, H. B. 1991, *ApJ*, 366, 455
 Lee, H. M. & Ostriker, J. P. 1987, *ApJ*, 322, 123
 Little, R. J. A. & Rubin, D. R., 1987, *Statistical Analysis with Missing Data* (New York: John Wiley & Sons, Inc.)
 Lynden-Bell, D. & Wood, R. 1968, *MNRAS*, 138, 495
 McLaughlin, D. E., Harris, W. E., & Hanes, D. A. 1994, *ApJ*, 422, 486
 Mihalas, D. & Binney, J. 1981, *Galactic Astronomy: Structure and Kinematics* (San Francisco: W. H. Freeman and Co.)
 Morrison, H. & Sarajedini, A. eds. 1996, *Formation of Galactic Halo... Inside and Out*, (Astr. Soc. Pacific: San Francisco)
 Murali, C. & Weinberg, M. D. 1996, *MNRAS*, submitted, <http://xxx.lanl.gov/abs/astro-ph/9604049> (Paper I)
 Murali, C. & Weinberg, M. D. 1996, *MNRAS*, submitted, <http://xxx.lanl.gov/abs/astro-ph/9602058> (Paper II)
 Norris, J. 1986, *ApJS*, 61, 667
 Ostriker, J. P., Spitzer, L., Jr. & Chevalier, R. 1972, *ApJL*, 176, L51
 Ostriker, J. P., Binney, J. J. & Saha, P. 1989, *MNRAS*, 241, 849
 Quinn, P. J., Hernquist, L. & Fullager, D. P. 1993, *ApJ*, 403, 74
 Searle, L. & Zinn, R. 1978, *ApJ*, 225, 357
 Sommer-Larsen, J. & Zhen, C., 1990, *MNRAS*, 242, 10
 Spitzer, L. Jr. 1940, *MNRAS*, 100, 396
 Spitzer, L. Jr. 1987, *Dynamical Evolution of Globular Clusters* (Princeton: Princeton University Press)
 Spitzer, L., Jr. & Chevalier, R. A. 1973, *ApJ*, 183, 565
 Stuart, A. & Ord, J. K. 1991, *Kendall's Advanced Theory of Statistics*, V.2 (London: Edward Arnold)
 Thomas, P. 1989, *MNRAS*, 238, 1319
 Tremaine, S. D. & Weinberg, M. W. 1984, *MNRAS*, 209, 729
 Wainscoat, R. J., Cohen, M., Volk, K., Walker, H. J. & Schwartz, D. E., 1992, *ApJS*, 83, 111
 Weinberg, M. D. 1994, *AJ*, 108, 1414
 Zinn, R. 1985, *ApJ*, 293, 424
 Zinn, R. 1993, in *The Globular-Cluster Galaxy Connection*, eds. Smith, G. H. & Brodie, J. P., (Astr. Soc. Pacific: San Francisco), 38
 Zinn, R. 1996, in *Formation of the Galactic Halo...Inside and Out*, eds. Morrison, H. & Sarajedini, A. (Astr. Soc. Pacific: San Francisco), 211

APPENDIX A: HEATING RATE FOR DISK OSCILLATIONS

Clusters confined to the disk oscillate about the midplane and are heated through resonance with the periodic tidal compression in the direction perpendicular to the disk plane. As discussed in Weinberg (1994), the tidal potential of the disk is well-approximated by the leading term of an expansion of the disk potential about the center of mass of the cluster:

$$H_1 = 2\pi G\rho[Z(t)]z^2, \quad (\text{A1})$$

where we have substituted the density for the second derivative of the disk potential using Poisson's equation. The quantity $Z(t)$ is the cluster position as a function of time, and z refers to the position of a star relative to the center of the cluster.

Expanding the z^2 factor in the action-angle Fourier series as defined in Tremaine & Weinberg (1984), we obtain

$$z^2 = \sum_{l=-\infty}^{\infty} \left[\frac{2}{3} \sqrt{\frac{4\pi}{5}} V_{2l20}(\beta) + \frac{1}{3} \sqrt{4\pi} V_{0l20}(\beta) \right] X_{l2}^{l1} e^{i l \cdot \mathbf{w}}. \quad (\text{A2})$$

Substituting the resulting expression for H_1 into equation (5) of Paper I, we derive the heating rate

$$\langle \dot{E} \rangle = -8\pi^4 P \frac{df}{dE} \sum_{l=-\infty}^{\infty} \delta_{l30} \left(\frac{1}{15} + \frac{1}{5} \delta_{l20} \right) (\mathbf{l} \cdot \boldsymbol{\Omega})^2 |X_{l2}^{l1}|^2 \sum_{n=-\infty}^{\infty} |a_n|^2 \delta(\mathbf{l} \cdot \boldsymbol{\Omega} - n\omega). \quad (\text{A3})$$

Choosing the vertical profile of the disk and the amplitude of vertical oscillations completely specifies the rate of energy input for given cluster profile. In the present work, we adopt a Gaussian vertical profile for the disk. Comparison with an exponential vertical profile reveals little difference in overall heating rate at any oscillation amplitude.

APPENDIX B: COORDINATE SYSTEMS

Our analysis uses three coordinate systems: heliocentric spherical coordinates, Galactocentric spherical coordinates and Galactocentric cylindrical coordinates. The first system is the natural observational reference frame while the second and third are the natural reference frames for the sphere and disk models, respectively. In the heliocentric frame, we use (r, l, b) or distance, Galactic longitude and Galactic latitude. In the Galactocentric spherical frame, we use the (R, Φ, Θ) to denote Galactocentric distance, colatitude and azimuth respectively. In the Galactocentric cylindrical frame, we use the (R_d, Φ, Z) to denote Galactocentric radius in the disk, azimuth and height above the plane, respectively.

Velocity components in a particular direction are denoted with the corresponding subscript. In the heliocentric frame, (v_r, v_l, v_b) are the radial, azimuthal and latitudinal components, respectively. In the Galactocentric spherical frame, (v_R, v_Φ, v_Θ) are the radial, azimuthal and latitudinal components, respectively. In the Galactocentric cylindrical frame, (v_{R_d}, v_Φ, v_Z) are the polar radial, azimuthal and vertical velocities, respectively. We also write the components in the equivalent inner product form so that, for example, the Heliocentric velocity components are $(\vec{v} \cdot \hat{r}, \vec{v} \cdot \hat{l}, \vec{v} \cdot \hat{b})$.

APPENDIX C: GENERALIZED MESTEL DISK

The phase space distribution function for disk clusters in the thin disk approximation has the form

$$\frac{\partial N}{\partial E_d \partial J_z^2 \partial E_z} = f_d(E_d, J_z^2) g(E_z) \quad (\text{C1})$$

where $f_d(E_d, J_z^2)$ governs the distribution in the plane of the disk, $g(E_z)$ governs the distribution perpendicular to the disk, E_d denotes orbital energy in the disk, J_z refers to the angular momentum along the Z-axis and E_z denotes the energy of vertical oscillations.

The Mestel disk distribution is defined as

$$f_d(E_d, J_z^2) = A e^{-E_d/\sigma_d^2} J_z^{2q_d}, \quad (\text{C2})$$

where σ_d^2 is the isothermal velocity dispersion in the disk. The radial and azimuthal velocity dispersions are $\sigma_{R_d}^2 = \sigma_d^2$ and $\sigma_\Phi^2 = (2q_d + 1)\sigma_d^2$ which implies $q_d = \sigma_\Phi^2/2\sigma_{R_d}^2 - \frac{1}{2}$, so that $-\frac{1}{2} \leq q_d \leq \infty$. The quantity q_d defines the anisotropy of the orbit distribution in the disk. For $q_d = -\frac{1}{2}$, the distribution has only radial orbits while as $q_d \rightarrow \infty$ the distribution has only circular orbits (Henon 1973; Barnes et al. 1986).

The isothermal vertical distribution is defined as

$$g(E_z) = B e^{-E_z/\sigma_z^2} \quad (\text{C3})$$

where σ_z^2 is the isothermal vertical velocity dispersion. In the Milky Way, σ_z^2 varies with radius in the disk because the scale height is constant while the midplane density varies. Assuming it to be fixed introduces some bias into the expected vertical velocities at a given radius. However, this has no effect on our conclusions because we find that heating by disk oscillations is nearly independent of oscillation amplitude (or, equivalently, velocity at the midplane; c.f. §3.1).

Integrating over v_{R_d} , v_Φ , v_Z and Z yields the surface density in the logarithmic potential

$$\frac{dN}{d^2R} = C \sqrt{\pi} (2\sigma_d)^{q+1} \Gamma(q + \frac{1}{2}) R_d^{-(\eta_d - 2q_d)} \quad (\text{C4})$$

where we absorb all vertical integration constants into the factor C and define the parameter $\eta_d = v_c^2/\sigma_d^2$. For $\eta_d - 2q_d = 2$, the density goes as $\ln R_d$.

APPENDIX D: GENERALIZED MESTEL SPHERE

The phase space distribution function for halo clusters has the form

$$\frac{\partial N}{\partial E \partial J^2} = f(E, J^2) \quad (\text{D1})$$

where E is the total energy and J is the total angular momentum of a cluster.

The Mestel sphere has the same form as the Mestel disk,

$$f(E, J^2) = A e^{-E/\sigma^2} J^{2q}, \quad (\text{D2})$$

but is a three-dimensional distribution so that the radial velocity dispersion $\sigma_R^2 = \sigma^2$ and tangential velocity dispersion $\sigma_T^2 = 2(q + 1)\sigma^2$. Consequently, $q = \sigma_T^2/2\sigma_R^2 - 1$ and $-1 \leq q \leq \infty$. The quantity q defines the anisotropy of the orbit distribution. For $q = -1$, the distribution has only of radial orbits while as $q \rightarrow \infty$ the distribution has only circular orbits (Henon 1973; Barnes et al. 1986). Integrating over v_R , v_Φ and v_Θ gives the volume density in the logarithmic potential

$$\frac{dN}{d^3R} = A \pi^{3/2} (2\sigma^2)^{q+3/2} \Gamma(q + 1) R^{-(\eta - 2q)} \quad (\text{D3})$$

where we define $\eta = v_c^2/\sigma^2$. For $\eta - 2q = 3$, the density goes as $\ln R$.

APPENDIX E: GENERALIZED EDDINGTON SPHERE

The Eddington model has the distribution function

$$f(E, J^2) = Ae^{-E/\sigma^2} e^{-J^2/2R_a^2\sigma^2}, \quad (\text{E1})$$

which implies that $\sigma_R^2 = \sigma^2$ and $\sigma_T^2 = 2\sigma^2/(1 + R^2/R_a^2)$. Integrating over velocities gives the volume density in the logarithmic potential

$$\frac{dN}{d^3R} = A2\pi(2\pi\sigma^2)^{3/2} \frac{R^{-\eta}}{1 + R^2/R_a^2} \quad (\text{E2})$$

where we define $\eta = v_c^2/\sigma^2$.

APPENDIX F: LIKELIHOOD WITH INCOMPLETE DATA SETS

An incomplete data set is defined as one in which some observations are missing. For each cluster, the observations have varying completeness with respect to the full set of observations required in a given model. There are several approaches to deriving parameter estimates in this situation. In the present work, we adopt a likelihood-based estimation scheme[‡].

If we denote the full phase-space vector for our models (\vec{r}, \vec{v}, m) as Y and write $Y = (Y_{obs}, Y_{mis})$, where Y_{obs} signifies the observed data and Y_{mis} signifies the missing data, then $f(Y|\vec{\theta}) = f(Y_{obs}, Y_{mis}|\vec{\theta})$ denotes the underlying probability of observing all quantities Y_{obs} and Y_{mis} , where $f(\cdot|\vec{\theta})$ is governed by the parameters $\vec{\theta}$. Integrating the distribution over each case of missing data gives the marginal probability density of Y_{obs} :

$$f(Y_{obs}|\theta) = \int f(y_{obs}, Y_{mis}|\vec{\theta}) dY_{mis}. \quad (\text{F1})$$

For independent observations, we denote the marginal probability for the i^{th} cluster as $f_i = f(Y_{i,obs}|\vec{\theta})$ and write the likelihood function in the usual way as the joint probability of the observations given the model:

$$L(\vec{\theta}) = \prod_i f_i. \quad (\text{F2})$$

Using $L(\vec{\theta})$ to derive inferences concerning $\vec{\theta}$ requires that there are no selection effects leading to the systematic absence of data for a particular class of observations. In practice, of course, we know that this is not the case for observations of globular clusters, where, for example, latitude-dependent extinction results in the absence of radial velocities. However, in the present analysis we make no attempt to derive any type of selection function. One approach which does not ignore selection effects is the *Expectation-Maximization* algorithm, an iterative procedure which provides estimates for the model parameters as well as the missing data (Little & Rubin 1987, ch. 7).

The standard data set used in analyses of the spatial distribution and kinematics of the cluster system consists of cluster positions, masses and heliocentric radial velocities

(Aguilar, Hut & Ostriker 1988; Thomas 1989). For example, if we take a spherical model for the cluster distribution function $f(E, J^2)$, the marginal probability of any given observation is

$$\bar{f}(v_r, R) = \int dv_l dv_b f\left(\frac{1}{2}(v_r^2 + v_l^2 + v_b^2) + \Psi(R), R^2((\vec{v} \cdot \hat{\Phi})^2 + (\vec{v} \cdot \hat{\Theta})^2)\right), \quad (\text{F3})$$

where $\Psi(R)$ is the potential, and the tangential velocity components are written in inner product notation.

[‡] The following discussion is based on the presentation of Little & Rubin (1987), chapter 5.